Check for updates

Instantaneous rock transformations in the deep crust driven by reactive fluid flow

A. Beinlich [1,2 ✉], T. John [3 ✉], J. C. Vrijmoed[3], M. Tominaga [4], T. Magna[5] and Y. Y. Podladchikov [6]

Fluid–rock interactions are a fundamental component of geodynamic processes. They link mass and energy transfer with large-scale tectonic deformation and drive mineral deposit formation, carbon sequestration and rheological changes of the lithosphere. Spatial evidence indicates that fluid–rock interactions operate on length scales that range from the grain boundary to tectonic plates, but the timescales of regional fluid–rock interactions remain essentially unconstrained. Here we present observations from an exceptionally well-exposed fossil hydrothermal system from an ophiolite sequence in northern Norway that we use to inform a multielement advection–diffusion–reaction transport model. We calculated the velocity of the fluid-driven reaction fronts and found that they can propagate at up to 10 cm per year, equivalent to the fastest tectonic plate motion and mid-ocean-ridge spreading rates. Propagation through the low-permeability rocks of the mid-crust is facilitated by a transient, reaction-induced permeability increase. We conclude that large-scale fluid-mediated rock transformations in continental collision and subduction zones occur on timescales of tens of years when reactive fluids are present. We infer that natural carbon sequestration, ore deposit formation and transient and long-term petrophysical changes of the crust proceed instantaneously, from a geological perspective.

Fluids fundamentally govern the physicochemical properties of the Earth's lithosphere by linking chemical reactions with the transport of mass and energy, and tectonic deformation[1]. As rock is inevitably altered in the presence of fluids, these interactions profoundly influence the crustal rheology[2], gravity and magnetic properties[3–6] and are frequently accompanied by the formation of hydrothermal ore deposits[7,8] and carbon sequestration[9], and have been linked to the emergence of life[10]. Although fluid–rock interactions operate on various length scales—from grain boundaries to outcrops to regional albitization and amphibolitization of continental terranes and finally even to pervasive serpentinization of the oceanic lithosphere[11]—the timescales of regional fluid–rock interactions remain essentially unconstrained, despite being critically significant for the dynamic evolution of the Earth's crust.

Given the durations of other geological processes, fluid–rock interactions probably occur on timescales between the long-lasting orogenic cycle[12–14] and slab fluid release[15–18] (Fig. 1); more precise constraints have been unattainable because suitable chronometers are lacking. Namely, conventional radiogenic dating techniques provide absolute ages instead of durations and their uncertainties are too large to capture fast and transient geological processes. Further, upscaling of experimentally derived reaction rates remains challenging[19–21]. Thus, to constrain the durations of regional fluid–rock interactions, sufficiently large natural systems must be investigated.

To quantify fluid–rock interaction durations, the feasible fluid advection velocities through the crust must be known. However, the small dimension of intra-crustal fluid pathways hampers a direct geophysical monitoring, and forward simulations based on extrapolating the measured rock permeability are subject to large uncertainties that arise from transient variations, such as those documented for shallow seismic events and geothermal system stimulations[15,22,23]. Furthermore, such transient variations probably also occur in the deeper crust, as inferred from preserved pore networks in exhumed metamorphic rocks, numerical simulations and time-integrated fluid-flux calculations[23–27].

Therefore, to quantify the duration of regional-scale fluid–rock interactions, here we first investigated the exceptional exposure of abundant and clearly defined, sharp reaction fronts that result from the fluid-driven alteration of serpentinite. These field relationships provide critical insights into the conditions and geometry of fluid migration, and the relatively simple composition of the ultramafic precursor offers a reduced complexity compared to that of other large multicomponent natural systems. Then, using the obtained parameters, we constrained the duration of fluid–rock interaction by fitting an innovative numerical model that couples reactive transport, mass conservation and local equilibrium thermodynamics with the mineral chemistry and abundance, and the composition of the hydrothermally altered rock.

Serpentinite alteration by reactive fluid flow

Our natural laboratory comprises a tectonically dismembered ophiolite situated within greenschist-to-lower amphibolite facies metamorphosed metasediments of the Caledonian Köli Nappe of northern Norway (Methods)[3,28]. About 20 individual ophiolite fragments are pervasively altered to a talc–magnesite–chlorite assemblage (soapstone) on the scale of several hundred cubic metres due to their reaction with carbon-bearing aqueous fluid[28]. Reaction fronts are sharp on both the outcrop and the thin section scales, and they are defined by the formation of the soapstone assemblage from a completely serpentinized precursor (Figs. 2a and 3a,b, Extended Data Fig. 1 and Supplementary Fig. 1). The presence of pervasively carbonated contact zones between the ophiolite and the underlying sedimentary schist indicates a local origin of the alteration fluid (Fig. 2b)[28], in which a carbon-bearing aqueous pore fluid is released

[1]Department of Earth Science, University of Bergen, Bergen, Norway. [2]The Institute for Geoscience Research (TIGeR), School of Earth and Planetary Sciences, Curtin University, Perth, Western Australia, Australia. [3]Institut für Geologische Wissenschaften, Freie Universität Berlin, Berlin, Germany. [4]Woods Hole Oceanographic Institution, Woods Hole, MA, USA. [5]Czech Geological Survey, Prague, Czech Republic. [6]Institute of Earth Sciences, University of Lausanne, Lausanne, Switzerland. ✉e-mail: andreas.beinlich@uib.no; timm.john@fu-berlin.de
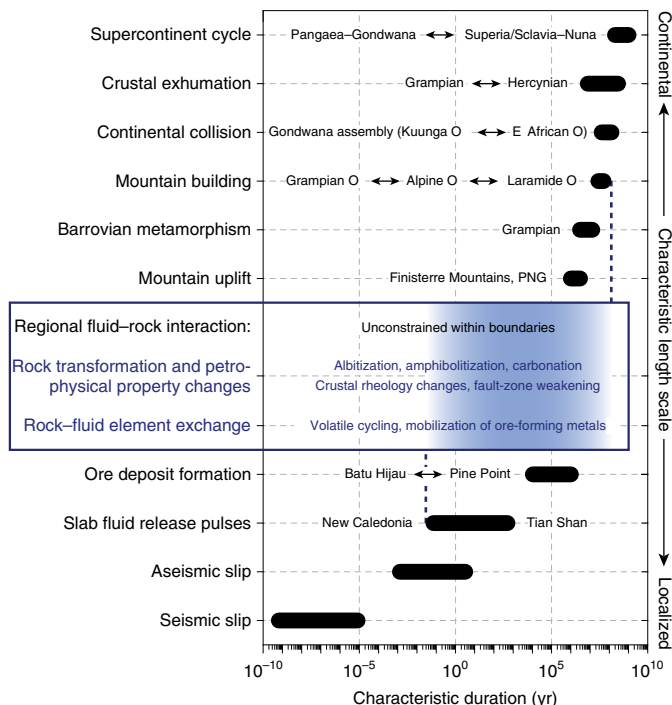
Fig. 1 | Characteristic durations and scales of geological processes.
The durations of fluid–rock interactions remain unconstrained between
orogenic processes and fluid release from subducting slabs. Data are
compiled from: supercontinent cycle[43], crustal exhumation[44,45], continental
collision[12], mountain building[13,14], Barrovian metamorphism[46], mountain
uplift[47], ore deposit formation[48,49], slab fluid release[15,16] and seismic and
aseismic slip[50]. E, East; O, orogeny; PNG, Papua New Guinea.

due to the compaction of the local sediments and/or the thermally
facilitated dissolution of carbonate during tectonic underthrusting
below the relatively hotter oceanic lithosphere (Fig. 2b)[29]. Additional
soapstone is present in reaction selvages along intra-ophiolite frac-
tures that are ten to several hundred metres long and connected to

the basal thrust, indicating the fractures functioned as fluid con-
duits (Fig. 2b). Importantly, one of these reaction selvages perfectly
exposes the field relationships, which allowed us to extract the nec-
essary parameters at the required precision to constrain the fluid–
rock interaction timescale via modeling (Extended Data Fig. 1).

Our observations and model input parameters are based on the
analyses of 17 core samples from a 5 m long transect across a 2.6 m
wide soapstone fracture selvage in serpentinite (Extended Data Fig. 1).
The texturally and compositionally homogeneous soapstone con-
tains on average 29 ± 5 vol% carbonate dominated by magnesite,
$17 \pm$ vol% chlorite and 48 ± 5 vol% talc (Supplementary Methods 2).
The modal contents of magnetite and relic serpentine inclusions in
carbonate are below 3 vol% (Fig. 3b, Supplementary Figs. 1 and 2 and
Supplementary Tables 1 and 2). A lithostatic pressure of ~300 MPa
is inferred from the alteration temperature of ~300 °C (ref. [28]) and a
thermobaric gradient of ~1 °C MPa^{-1}.

Reactive transport local equilibrium model

In our numerical model, serpentinite is replaced by soapstone along
the one-dimensional (1D) fluid infiltration path perpendicular to
the central fracture in response to the advective–diffusive transport
of carbon, silica and lithium through interconnected pore space
(Fig. 3c, Methods and Extended Data Fig. 1). The carbon concen-
tration of the input fluid is low (CO_2 ~1 wt%), consistent with the
composition of natural fluids, thermodynamic predictions and
experimental observations[28,30,31], and aqueous silica is derived from
serpentine dissolution along the flow path. Changes of fluid and
solid compositions are controlled by mineral replacement in accor-
dance with local equilibrium thermodynamics and mass conserva-
tion. Thus, mineral proportions and chemistry vary in response
to the dynamically changing system composition, and the model
reproduces the observed mineral proportions and compositions
(Methods). Using the known diffusion coefficient, fluid and rock
densities, and length scales, we minimized the mismatch between
the observed and modelled data, and thus reproduced the observed
front sharpness by varying the advective fluid flux relative to carbon
diffusion in the aqueous fluid. Generally, a faster fluid advection
increased the sharpness and propagation rate of the reaction front.
This unique approach constrains the alteration duration to $20 \pm^{9}_{5}$
years, equivalent to a surprisingly fast average front propagation
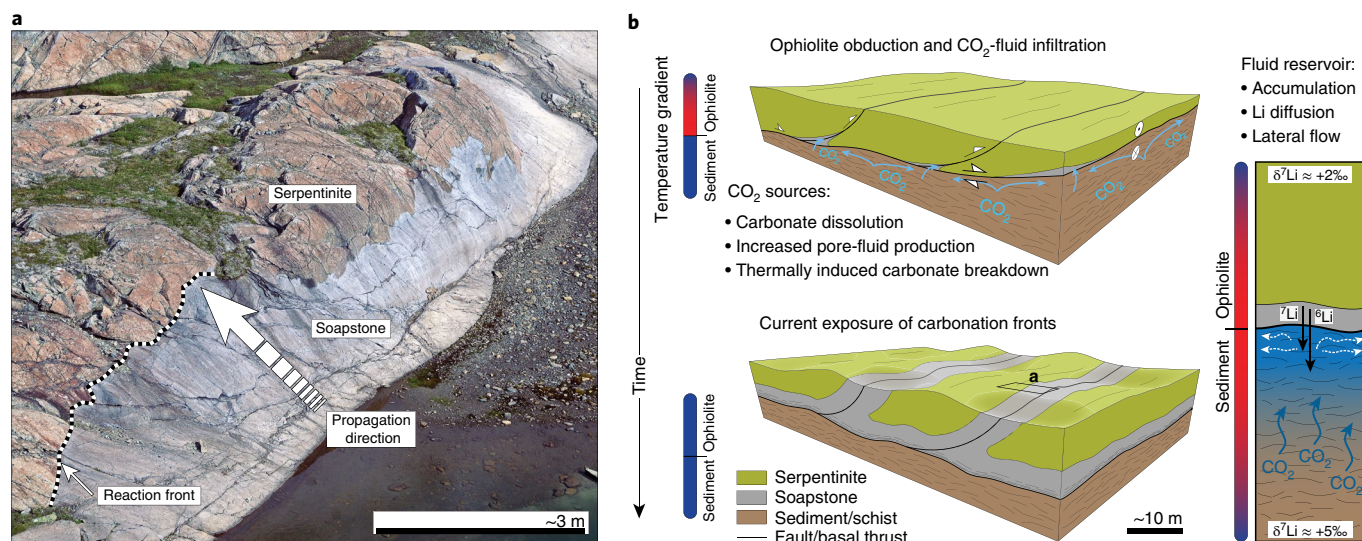
Fig. 2 | Ophiolite obduction and alteration. a, Representative outcrop image of a ~3 m wide soapstone alteration selvage around a fracture in serpentinite.
b, Schematic depicting ophiolite emplacement onto metasediments, alteration fluid accumulation below the basal ophiolite thrust and soapstone formation
along the thrust and fluid conduits. Lithium isotope exchange during incipient alteration across the tectonic contact controls the lithium budget of the
alteration fluid reservoir. The temperature gradients illustrate the thermal evolution of the system during and after ophiolite obduction and alteration.

rate of ~0.13 m yr^{-1} (Fig. 3c; see Methods for the discussion of the model uncertainty). The obtained front propagation rate is orders of magnitude faster than that inferred from retrograde metamorphic reactions at high temperature but fluid-starved conditions[19] and is at least as fast as the fastest current tectonic plate motion.

Constraints from Li isotope systematics

This calculated duration of the reaction front propagation is consistent with the measured variation of bulk rock lithium concentrations and isotope ratios (δ^7Li), which are known to accompany short fluid–rock interaction processes[15,16]. Lithium concentrations in the soapstone gradually decrease from the reaction interface towards the vein, whereas lithium isotope ratios are high near the vein (δ^7Li = 4.9‰), slightly lower in the precursor serpentinite (δ^7Li ≤ 2.2‰), and show a significant deviation to negative values (δ^7Li = −4.5‰) in the centre of the reaction selvage (Fig. 4a and Supplementary Table 3). Lithium solid-state diffusion is slow at mid-crustal temperatures. Hence, the outcrop-scale variation in lithium isotope ratios can only result from the faster diffusivity of ^{6}Li relative to ^{7}Li during fluid-mediated transport after lithium is released from antigorite, but before lithium is taken up by secondary chlorite and talc. However, the mass transport efficiency during reactive fluid flow is controlled by the fluid–solid mass transfer. Elements that more strongly partition into the solid are chemically retarded relative to those that partition less strongly into the solid. Available partition coefficients indicate that lithium concentrations are generally lower in the solid than in the respective equilibrium fluid, whereas measured carbon concentrations in the soapstone are approximately ten times higher than those in the equilibrium fluid (Extended Data Fig. 2a and Supplementary Methods 3.1). Hence, carbon transport and propagation of the reaction front are retarded relative to the transport of lithium, and lithium released by the reaction at the front will be transported downstream instead of being incorporated in talc and chlorite. Consequently, the observed systematic trend in the δ^7Li variation over time can only reflect fluid compositional changes that are controlled by reactions outside the sample transect that occur at large scales (Fig. 4b,c). In contrast to the relatively small-scale fracture reaction selvages within the ophiolite, the fluid–rock interaction occurs on a much larger scale along the tectonic contact with the underlying sedimentary schist, where we observe consistently pervasive thrust-parallel soapstone alteration (Fig. 2b, Methods and Extended Data Fig. 5). Predominantly horizontal fluid reservoir drainage into the tectonic fluid conduits within the ophiolite has only a minor influence on the composition of the alteration fluid (Fig. 4c). Thus, we attribute the variation of δ^7Li along the investigated transect to a large-scale diffusive lithium exchange between the antigorite dehydration fluid and the sediment-hosted fluid (Fig. 4a).

Consequences of fast reaction front propagation

Another intriguing aspect of the modelling approach is that it allows us to evaluate the implicitly changing permeability based on a simple Darcy relationship and assuming a buoyancy-driven hydraulic gradient ($\nabla P = g \times (\rho_{fluid} - \rho_{solid})$) of about −19 MPa km^{-1} (ref. [24]). The model input flux that results in the best fit of the modelled-to-measured antigorite abundance (equivalent to the fluid–rock interaction duration of ~20 years) is 20.4 m yr^{-1}. This implies a permeability, κ, of ~10$^{-14.5}$ m^2 during the reaction front propagation, which is high compared to the measured permeability of the least-carbonated serpentinite of ~10^{-17} m^2 (Supplementary Table 2) and that of antigorite from another location ($\kappa \approx 10^{-20}$ m^2) (ref. [32]). However, similarly high values have been hypothesized to occur transiently during fluid-driven metamorphic reactions despite the lack of robust timescale constraints[23]. Fitting the modelled-to-measured antigorite abundance by using the measured permeability ($\kappa \approx 10^{-17}$ m^2) requires an unrealistically strong hydraulic gradient, ~2.5 orders of
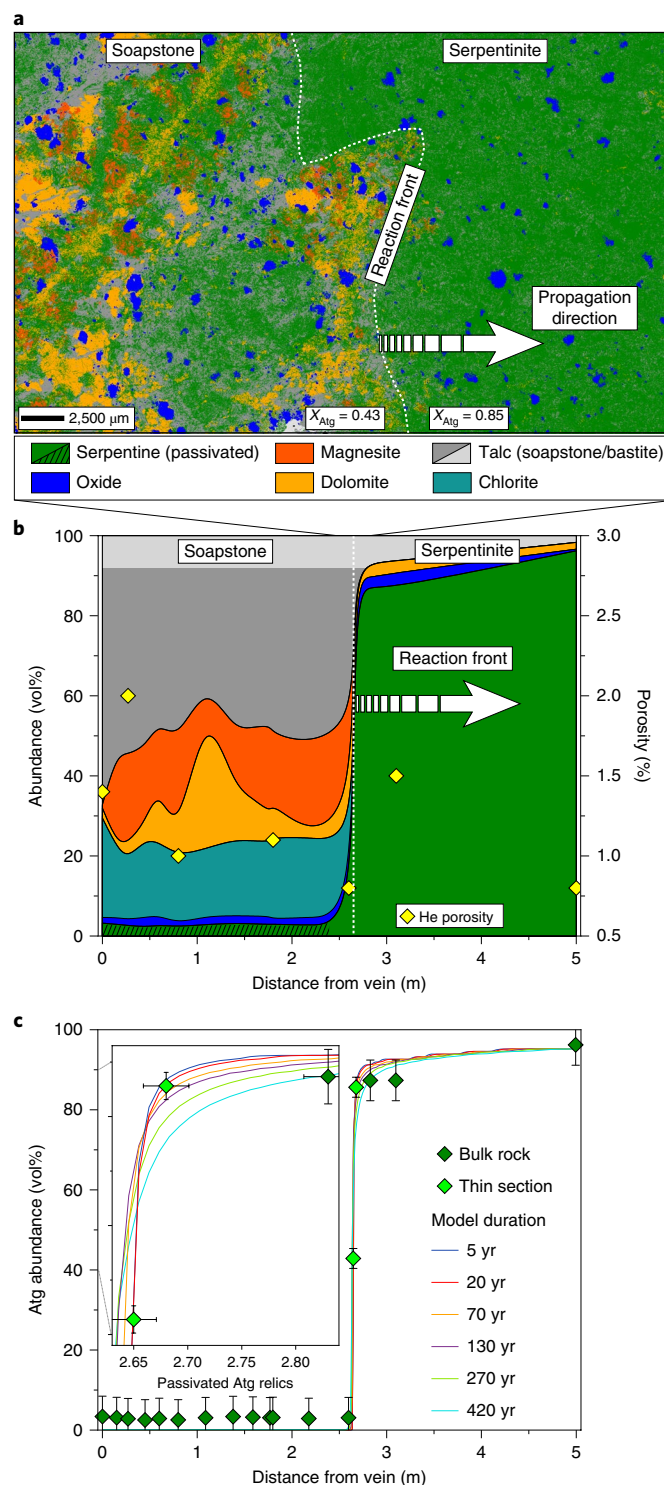
Fig. 3 | Mineral replacement during serpentinite alteration. a, Mineral distribution map across the reaction interface. **b,** Bulk rock mineral abundance across the reaction interface. Talc in serpentinite is a relic from earlier pyroxene. Serpentine in soapstone occurs as inclusions in magnesite (Supplementary Fig. 1c). **c,** The reactive transport model fitted to measured antigorite volume fractions for different alteration durations. Vertical error bars denote a 10% uncertainty of the bulk rock data and a 5% uncertainty of the thin section data. The uncertainty of the measured sample locations is the drill core diameter. The distance uncertainty of the thin section data is the half-width from each end. Atg, antigorite.
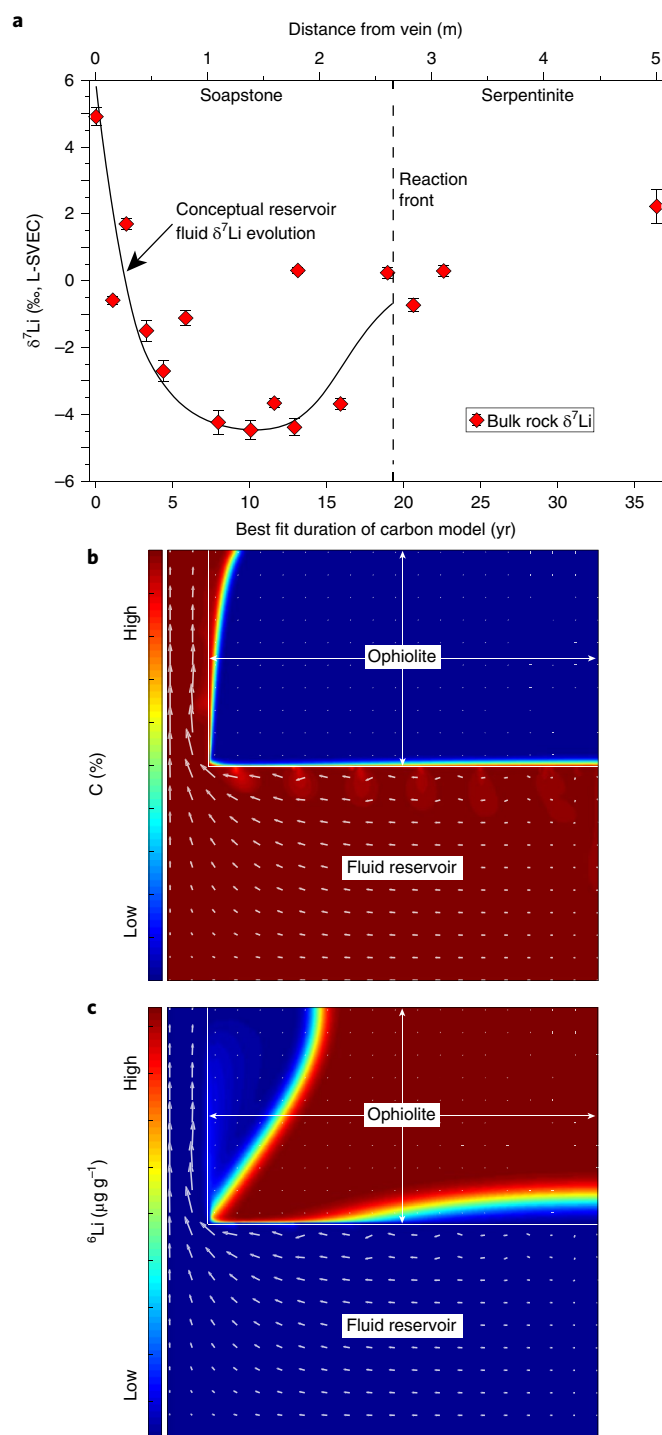
Fig. 4 | Outcrop lithium isotope distribution and fluid reservoir compositional evolution. a, Bulk rock lithium isotope distribution in outcrop and conceptual reservoir fluid δ⁷Li evolution during diffusive isotope exchange between the ophiolite- and sediment-hosted alteration fluid (see also panel **c**, Fig. 2b and Extended Data Fig. 5). The bottom abscissa shows the timescale obtained from the reactive transport model. Error bars indicate the 2σ analytical uncertainty. **b**, Fluid carbon concentrations and flow vectors in 2D. Beneath the basal thrust, flow is predominantly horizontal and drains the top section of the fluid reservoir into the ophiolite-hosted vertical fracture. Fluid density gradients result in deviation from a purely horizontal flow. **c**, Fluid ⁶Li concentrations in 2D, showing that mineral replacement lags behind the fluid ⁶Li front.

magnitude higher than that derived from the fluid–solid buoyancy contrast. Hence, we interpret the calculated permeability as a transient, reaction-induced corollary of front propagation.

The presence of abundant and large-scale soapstone alteration within an area of ~70 km² (ref. [28]) indicates a pervasive fluid–rock interaction at the regional scale, facilitated by the concomitant alteration at multiple structurally controlled reaction zones. Soapstone–serpentinite fronts are consistently sharp throughout the entire field area, and front propagation distances from identifiable fluid conduits typically vary between a few centimetres and several tens of metres, but the fronts lack evidence for repeated fluid infiltration, such as overprinting of pre-existing fronts and cross-cutting relationships. Hence, we infer that the calculated front propagation velocity (0.13 m yr⁻¹) is also applicable at the field scale, which implies a regional-scale alteration duration on the order of 10–100 years. The parameters of our numerical simulation are consistent with the background permeability, fluid composition and pressure and temperature conditions of the deeper crust irrespective of local lithology. Moreover, in our model hydrous serpentinite is altered by an aqueous fluid that contains ≤1 wt% CO_2 and the rock alteration driving force is probably higher for the alteration of anhydrous high grade metamorphic and igneous rocks with aqueous and ore forming hydrothermal fluid[8,11,33,34]. Hence, the characteristic timescale of fluid–rock interaction in such systems may be even shorter and may further decrease at higher temperatures in the lower crust.

Our data indicate that fluid-mediated rock alteration fronts propagate at least at the same rate as large-scale tectonic processes, including mid-ocean ridge spreading, plate motion and subduction[35–37]. Consequently, fluid-mediated changes in the physical properties of rock also proceed, from a geodynamic perspective, instantaneously. This not only has important implications for the rates of rheology, gravity and magnetic character changes of the newly formed oceanic lithosphere exposed to hydrothermal seawater circulation along mid-ocean ridges[3,5,38], but also justifies the assumption of instantaneous rock equilibration in large-scale geodynamic models that link, for example, far-field crustal deformation to differences in rheologic properties[2,39,40]. Moreover, fast fluid–solid reactions may explain the progressive propagation of tectonic relaxation fronts and the transient nature of episodic tremor and slip that have been related to localized near-lithostatic fluid pressure[41,42]. Our data directly show that carbon uptake in ultramafic rock takes place on timescales of tens to hundreds of years. If ophiolites are repeatedly infiltrated by carbon-bearing fluid over a sufficiently long timescale, they may represent effective sinks in the long-term carbon cycle. Finally, if the timescales of hydrothermal ore deposit formation are equally short, fluid–rock interactions actively recharge the crustal endowment in mineral commodities on timescales relevant for the resources demand of future generations.

Online content

Any methods, additional references, Nature Research reporting summaries, source data, extended data, supplementary information, acknowledgements, peer review information; details of author contributions and competing interests; and statements of data and code availability are available at https://doi.org/10.1038/s41561-020-0554-9.

References

1. Jamtveit, B., Austrheim, H. & Malthe-Sørenssen, A. Accelerated hydration of the Earth's deep crust induced by stress perturbations. *Nature* **408**, 75–78 (2000).
2. Bürgmann, R. & Dresen, G. Rheology of the lower crust and upper mantle: evidence from rock mechanics, geodesy, and field observations. *Annu. Rev. Earth Planet. Sci.* **36**, 531–567 (2008).

3. Tominaga, M. et al. Multi-scale magnetic mapping of serpentinite carbonation. *Nat. Commun.* **8**, 1870 (2017).

4. Maffione, M., Morris, A., Plümper, O. & van Hinsbergen, D. J. J. Magnetic properties of variably serpentinized peridotites and their implication for the evolution of oceanic core complexes. *Geochem. Geophys. Geosyst.* **15**, 923–944 (2014).

5. Toft, P. B., Arkani-Hamed, J. & Haggerty, S. E. The effects of serpentinization on density and magnetic susceptibility: a petrophysical model. *Phys. Earth Planet. Inter.* **65**, 137–157 (1990).

6. Bostock, M. G., Hyndman, R. D., Rondenay, S. & Peacock, S. M. An inverted continental Moho and serpentinization of the forearc mantle. *Nature* **417**, 536–538 (2002).

7. Beinlich, A., Dipple, G. M., Barker, S. L. L., Hansen, L. D. & Megaw, P. K. M. Large-scale stable isotope alteration around the hydrothermal carbonate-replacement Cinco de Mayo Zn–Ag deposit, Mexico. *Econ. Geol.* **114**, 375–396 (2019).

8. Hedenquist, J. W. & Lowenstern, J. B. The role of magmas in the formation of hydrothermal ore deposits. *Nature* **370**, 519–527 (1994).

9. Kelemen, P. B. & Matter, J. In situ carbonation of peridotite for CO_2 storage. *Proc. Natl Acad. Sci. USA* **105**, 17295–17300 (2008).

10. Martin, W., Baross, J., Kelley, D. & Russell, M. J. Hydrothermal vents and the origin of life. *Nat. Rev. Microbiol.* **6**, 805–814 (2008).

11. Engvik, A. K., Putnis, A., Fitz Gerald, J. D. & Austrheim, H. Albitization of granitic rocks: the mechanism of replacement of oligoclase by albite. *Can. Mineral.* **46**, 1401–1415 (2008).

12. Meert, J. G. A synopsis of events related to the assembly of eastern Gondwana. *Tectonophysics* **362**, 1–40 (2003).

13. Viete, D. R., Oliver, G. J. H., Fraser, G. L., Forster, M. A. & Lister, G. S. Timing and heat sources for the Barrovian metamorphism, Scotland. *Lithos* **177**, 148–163 (2013).

14. Whitney, D. L., Miller, R. B. & Paterson, S. R. P–T–t evidence for mechanisms of vertical tectonic motion in a contractional orogen: northwestern US and Canadian Cordillera. *J. Metamorph. Geol.* **17**, 75–90 (1999).

15. John, T. et al. Volcanic arcs fed by rapid pulsed fluid flow through subducting slabs. *Nat. Geosci.* **5**, 489–492 (2012).

16. Taetz, S., John, T., Bröcker, M., Spandler, C. & Stracke, A. Fast intraslab fluid-flow events linked to pulses of high pore fluid pressure at the subducted plate interface. *Earth Planet. Sci. Lett.* **482**, 33–43 (2018).

17. Dragovic, B., Baxter, E. F. & Caddick, M. J. Pulsed dehydration and garnet growth during subduction revealed by zoned garnet geochronology and thermodynamic modeling, Sifnos, Greece. *Earth Planet. Sci. Lett.* **413**, 111–122 (2015).

18. Dragovic, B., Gatewood, M. P., Baxter, E. F. & Stowell, H. H. Fluid production rate during the regional metamorphism of a pelitic schist. *Contrib. Mineral. Petrol.* **173**, 96 (2018).

19. Baxter, E. F. & DePaolo, D. J. Field measurement of slow metamorphic reaction rates at temperatures of 500° to 600 °C. *Science* **288**, 1411–1414 (2000).

20. Cushman, J. H. On measurement, scale, and scaling. *Water Resour. Res.* **22**, 129–134 (1986).

21. White, A. F. & Brantley, S. L. The effect of time on the weathering of silicate minerals: why do weathering rates differ in the laboratory and field? *Chem. Geol.* **202**, 479–506 (2003).

22. Hanson, R. B. Effects of fluid production on fluid flow during regional and contact metamorphism. *J. Metamorph. Geol.* **10**, 87–97 (1992).

23. Ingebritsen, S. E. & Manning, C. E. Permeability of the continental crust: dynamic variations inferred from seismicity and metamorphism. *Geofluids* **10**, 193–205 (2010).

24. Manning, C. E. & Ingebritsen, S. E. Permeability of the continental crust: implications of geothermal data and metamorphic systems. *Rev. Geophys.* **37**, 127–150 (1999).

25. Plümper, O. et al. Fluid-driven metamorphism of the continental crust governed by nanoscale fluid flow. *Nat. Geosci.* **10**, 685–690 (2017).

26. Bickle, M. & Baker, J. Migration of reaction and isotopic fronts in infiltration zones: assessments of fluid flux in metamorphic terrains. *Earth Planet. Sci. Lett.* **98**, 1–13 (1990).

27. Skelton, A. Flux rates for water and carbon during greenschist facies metamorphism. *Geology* **39**, 43–46 (2011).

28. Beinlich, A., Plümper, O., Hövelmann, J., Austrheim, H. & Jamtveit, B. Massive serpentinite carbonation at Linnajavri, N–Norway. *Terra Nova* **24**, 446–455 (2012).

29. Menzies, C. D. et al. Carbon dioxide generation and drawdown during active orogenesis of siliciclastic rocks in the Southern Alps, New Zealand. *Earth Planet. Sci. Lett.* **481**, 305–315 (2018).

30. Graham, C. M., Greig, K. M., Sheppard, S. M. F. & Turi, B. Genesis and mobility of the H_2O–CO_2 fluid phase during regional greenschist and epidote amphibolite facies metamorphism: a petrological and stable isotope study in the Scottish Dalradian. *J. Geol. Soc.* **140**, 577–599 (1983).

31. Sieber, M. J., Hermann, J. & Yaxley, G. M. An experimental investigation of C–O–H fluid-driven carbonation of serpentinites under forearc conditions. *Earth Planet. Sci. Lett.* **496**, 178–188 (2018).

32. Katayama, I., Terada, T., Okazaki, K. & Tanikawa, W. Episodic tremor and slow slip potentially linked to permeability contrasts at the Moho. *Nat. Geosci.* **5**, 731–734 (2012).

33. Austrheim, H. Eclogitization of lower crustal granulites by fluid migration through shear zones. *Earth Planet. Sci. Lett.* **81**, 221–232 (1987).

34. Weis, P., Driesner, T. & Heinrich, C. A. Porphyry–copper ore shells form at stable pressure–temperature fronts within dynamic fluid plumes. *Science* **338**, 1613–1616 (2012).

35. Müller, R. D., Sdrolias, M., Gaina, C. & Roest, W. R. Age, spreading rates, and spreading asymmetry of the world's ocean crust. *Geochem. Geophys. Geosyst.* **9**, Q04006 (2008).

36. DeMets, C., Gordon, R. G., Argus, D. F. & Stein, S. Current plate motions. *Geophys. J. Int.* **101**, 425–478 (1990).

37. Stern, R. J. Subduction zones. *Rev. Geophys.* **40**, 1012 (2002).

38. Escartín, J., Hirth, G. & Evans, B. Effects of serpentinization on the lithospheric strength and the style of normal faulting at slow-spreading ridges. *Earth Planet. Sci. Lett.* **151**, 181–189 (1997).

39. Ranalli, G. & Murphy, D. C. Rheological stratification of the lithosphere. *Tectonophysics* **132**, 281–295 (1987).

40. Stüwe, K. *Geodynamics of the Lithosphere* (Springer, 2007).

41. Gomberg, J. & Group, C. W. Slow-slip phenomena in Cascadia from 2007 and beyond: a review. *Geol. Soc. Am. Bull.* **122**, 963–978 (2010).

42. Shelly, D. R., Beroza, G. C. & Ide, S. Non-volcanic tremor and low-frequency earthquake swarms. *Nature* **446**, 305–307 (2007).

43. Condie, K., Pisarevsky, S. A., Korenaga, J. & Gardoll, S. Is the rate of supercontinent assembly changing with time? *Precambrian Res.* **259**, 278–289 (2015).

44. Oliver, G. J. H., Chen, F., Buchwaldt, R. & Hegner, E. Fast tectonometamorphism and exhumation in the type area of the Barrovian and Buchan zones. *Geology* **28**, 459–462 (2000).

45. Graessner, T., Schenk, V., Bröcker, M. & Mezger, K. Geochronological constraints on the timing of granitoid magmatism, metamorphism and post-metamorphic cooling in the Hercynian crustal cross-section of Calabria. *J. Metamorph. Geol.* **18**, 409–421 (2000).

46. Baxter, E. F., Ague, J. J. & DePaolo, D. J. Prograde temperature–time evolution in the Barrovian type—locality constrained by Sm/Nd garnet ages from Glen Clova, Scotland. *J. Geol. Soc.* **159**, 71–82 (2002).

47. Abbott, L. D. et al. Measurement of tectonic surface uplift rate in a young collisional mountain belt. *Nature* **385**, 501–507 (1997).

48. McInnes, B. I. A., Evans, N. J., Fu, F. Q. & Garwin, S. Application of thermochronology to hydrothermal ore deposits. *Rev. Mineral. Geochem.* **58**, 467–498 (2005).

49. Garven, G. The role of regional fluid flow in the genesis of the Pine Point Deposit, Western Canada sedimentary basin. *Econ. Geol.* **80**, 307–324 (1985).

50. Peng, Z. & Gomberg, J. An integrated perspective of the continuum between earthquakes and slow-slip phenomena. *Nat. Geosci.* **3**, 599–607 (2010).

Methods

Geological context and field relationships. The Linnajavri field area is centred around 67° 36′ N and 16° 24′ E and contains ~20 individual ultramafic bodies distributed over an area of ~70 km^2 (ref. [51]). The area of individual ultramafic bodies, as exposed at the surface, ranges between several 100 m^2 to a few km^2. In the field, ultramafic bodies cluster in both a northern and a southern zone, the former of which is part of the Čohkul Nappe and contains the investigated outcrop, whereas the southern zone is part of the Ridoalggičohkka Nappe. In the Ridoalggičohkka Nappe, ultramafic rocks are underlain by carbonate–mica schist and subordinate calcite–dolomite marble, thin layers of quartzite, garnet-bearing mica schist and semi-concordant trondhjemite sills. The northern Čohkul Nappe is composed of garnet–mica schist and metagreywacke. Both napps are gently folded and most of the ultramafic bodies are present in the central parts of large synclinal structures[51]. Both local nappes are part of the regional Köli Nappe, which has been described as a sequence of Cambrian to Silurian oceanic metasediments that comprise calcareous psammite and pelite. The Köli Nappe is part of the Upper Allochthon of the Caledonian tectonostratigraphy[52,53]. In a few other places, the Köli Nappe has been further subdivided into several subunits and in these other sites ophiolite fragments are typically found in the lowermost subunits above the contact with the underlying Seve Nappe[54]. The metamorphic grade of the Köli Nappe is mostly greenschist facies and an upward increase to lower amphibole facies has been documented from the Nordhallen area of west-central Sweden[54,55].

The least-altered rock type in all the investigated ultramafic bodies is serpentinite and primary pyroxene and olivine have not been found[3,28,51]. The northern zone contains soapstone and serpentinite and the southern zone contains additional mafic rocks, which include pillow basalts, and listvenite along the basal thrust of the ultramafic bodies, that is, the quartz–magnesite alteration assemblage. The alteration of serpentinite to soapstone and listvenite is consistent with the infiltration of a carbon-bearing reactive fluid and does not require additional silica and other components[3,9,28,56,57]. Based on a conservative depth extrapolation, the total volume of soapstone at Linnajavri has been estimated as ~100 Mt but may be 2–3 times larger[51]. The alteration features and composition of serpentinite and soapstone are consistent throughout the field area. Serpentinite alteration is most strongly developed along the basal thrust of the ultramafic bodies and can be followed along fractures as reaction selvages into the interior parts of the ultramafic bodies. The reaction fronts shown in Fig. 2a and Extended Data Fig. 1 are representative of the front sharpness in the entire field area. In the field, soapstone can appear grey and rust brown, the latter of which is attributed to a more intense weathering and less mechanical erosion during the recent glaciation of the area. However, surface weathering is restricted to the outermost ~5 mm and the soapstone composition is invariant below the weathered surface. Despite the small degree of surface weathering, the location shown in Extended Data Fig. 1 was chosen for this study as it most clearly shows the relationship between the fluid conduit, alteration selvage and precursor serpentinite, and allowed for precise distance measurements.

Local equilibrium thermodynamic model. The multicomponent ultramafic system is approximated in the SiO$_2$–Al$_2$O$_3$–MgO–FeO–CaO–H$_2$O–CO$_2$ compositional space. Phase equilibria were calculated for 300 °C and 300 MPa, consistent with the previous temperature estimate and a geothermobaric gradient of 1 °C MPa^{-1} (ref. [28]). Furthermore, all the calculations were conducted using the system composition specified by element concentrations. To define a subspace of the entire compositional spectrum for the thermodynamic calculations, we precomputed all the possible compositional variations that may result from the fluid–rock interaction and subsequently focused on the relevant reactions that are informed by field observations and sample petrography. The critical reaction for the formation of soapstone from serpentinite is the dissolution of antigorite during the addition of CO$_2$ to form magnesite and talc:

$$2 \underbrace{Mg_3Si_2O_5(OH)_4}_{\text{serpentine}} + 3\,CO_{2,aq} \rightarrow 3\,\underbrace{MgCO_3}_{\text{magnesite}} + \underbrace{Mg_3Si_4O_{10}(OH)_2}_{\text{talc}} + 3\,H_2O \qquad (1)$$

Furthermore, the absence of quartz provides an upper limit for the alteration-fluid carbon concentration, above which serpentine alteration would form the assemblage magnesite + quartz (listvenite)[28]. Sample petrography also defines the composition of the starting material as a mixture of antigorite and dolomite without additional fluid (Lin_31; Supplementary Tables 1 and 2)[28]. Based on this composition, the critical elements that vary by dissolution and solute transport are carbon and silica. Hence, the compositional space is reduced to 2D. Charge balance constrains the amount of oxygen in the bulk composition, assuming all the Fe is ferrous, consistent with the absence of haematite and goethite from the samples.

For the calculations, we used solid-solution models for olivine (O(HP)), spinel (Sp(HP)), antigorite (Atg(PN)), brucite (B), magnesite (M(HP)), talc (T), chlorite (Chl(HP)), dolomite (Do(HP)), clinopyroxene (Omph(GHP)) and amphibole (Amph(DPW))[58–62] together with the thermodynamic dataset of Holland and Powell[58]. For the fluid phase we used the H$_2$O–CO$_2$ mixing model by Aranovich and Newton[63] with the H$_2$O and CO$_2$ endmembers derived from the CORK EOS of Holland and Powell[64]. This model was extended to include the aqueous silica endmember[58], which closely reproduced the quartz solubility experiments[65]. The mixing with aqueous silica was only done for the dilute limit in which

we took an ideal mixing approximation. Recent experimental evidence indicates that this modelling approach very closely reproduces phase equilibria in ultramafic systems in the presence of C–O–H fluids[31]. All the calculations were done in MATLAB following the methodology described in Vrijmoed and Podladchikov[66] and Plümper et al.[67].

We calculated the change in system composition and mineral abundance by independently varying the concentration of carbon between 0 and 1 mol% (Extended Data Fig. 2). Both the bulk system composition and the mineral abundance gradually changed with increasing carbon content, so that modes of talc and magnesite increased with decreasing antigorite content and chlorite stabilizes at a high carbon content just before antigorite reacted out. Our model accurately reproduces measured mineral compositions (Extended Data Fig. 3)[28]. The concentration of the system components in individual phases with increasing bulk system carbon content is shown in Extended Data Fig. 4. The thermodynamic calculations thus yield bulk rock and fluid densities, total volatile (CO$_2$ + H$_2$O) weight fractions in the solid and bulk solid carbon concentration for the T, P, C_{fluid} space of interest. These are the local thermodynamic closing relations for the reactive transport calculation, as discussed below.

Reactive transport model. The advection–diffusion–reaction model is based on local thermodynamic equilibrium and mass conservation at the propagating replacement front. Replacement of serpentinite by soapstone proceeds as a coupled carbonation and partial dehydration reaction. The conservation of both fluid and solid mass is expressed as:

$$\frac{\partial}{\partial t}\left(\rho_f \phi + \rho_s(1-\phi)\right) + \nabla\left(\rho_f \phi \mathbf{V}_f + \rho_s(1-\phi)\mathbf{V}_s\right) = 0 \qquad (2)$$

where ρ_s is the solid density, ρ_f the fluid density, ϕ the fluid-filled porosity, $\mathbf{V}_f$ the fluid velocity and $\mathbf{V}_s$ the solid velocity. The conservation of immobile solid mass is implemented by using:

$$\frac{\partial}{\partial t}\left(\rho_s(1-C_s^m)(1-\phi)\right) + \nabla\left(\rho_s(1-C_s^m)(1-\phi)\mathbf{V}_s\right) = 0 \qquad (3)$$

where C_s^m is the weight fraction of mobile oxides (weight fractions of H$_2$O, CO$_2$ and SiO$_2$) of the total solid rock mass. The mass conservation of total fluid and solid CO$_2$ is expressed as:

$$\frac{\partial}{\partial t}\left(\rho_f \phi C_f^{CO_2} + \rho_s(1-\phi)C_s^{CO_2}\right) + \nabla\left(\rho_f \phi C_f^{CO_2}\mathbf{V}_f + \rho_s(1-\phi)C_s^{CO_2}\mathbf{V}_s\right) = \nabla\left(\rho_f \phi D_f^{CO_2}\nabla C_f^{CO_2}\right) \qquad (4)$$

where $D_f^{CO_2}$ is the diffusion coefficient of CO$_2$ in aqueous fluid (Supplementary Methods 3.1), and $C_f^{CO_2}$ and $C_s^{CO_2}$ are the mass fractions of CO$_2$ in the fluid and solid, respectively. Adopting and substituting Darcy's permeability:

$$\phi(\mathbf{V}_f - \mathbf{V}_s) = -\frac{k\phi^3}{\mu_f}\left(\nabla P_f + \rho_f \mathbf{g}\right) \qquad (5)$$

where k is the permeability coefficient in a Kozeny–Carman-type permeability expression, μ_f the fluid viscosity, P_f the fluid pressure and $\mathbf{g}$ the gravitational acceleration. Assuming and substituting zero solid velocity:

$$\mathbf{V}_s = 0 \qquad (6)$$

into the mass conservation equations eliminates the velocities and results in three equations for three unknown fields that evolve in time and space, namely, reaction-induced fluid-filled porosity ϕ, fluid pressure P_f and the fluid CO$_2$ mass fraction $C_f^{CO_2}$:

$$\begin{cases} \frac{\partial}{\partial t}\left(\rho_f \phi C_f^{CO_2} + \rho_s(1-\phi)C_s^{CO_2}\right) - \nabla\left(\rho_f \phi C_f^{CO_2}\frac{k\phi^3}{\mu_f}(\nabla P_f + \rho_f \mathbf{g})\right) \\ = \nabla\left(\rho_f \phi D_f^{CO_2}\nabla C_f^{CO_2}\right) \\ \frac{\partial}{\partial t}\left(\rho_s(1-C_s^m)(1-\phi)\right) = 0 \\ \frac{\partial}{\partial t}\left(\rho_f \phi + \rho_s(1-\phi)\right) = \nabla\left(\rho_f \frac{k\phi^3}{\mu_f}(\nabla P_f + \rho_f \mathbf{g})\right) \end{cases} \qquad (7)$$

The closing relationships for the four remaining variables are derived from equilibrium thermodynamics:

$$\begin{cases} \rho_f = \rho_f\left(T, P_f, C_f^{CO_2}\right) \\ \rho_s = \rho_s\left(T, P_f, C_f^{CO_2}\right) \\ C_s^m = C_s^m\left(T, P_f, C_f^{CO_2}\right) \\ C_s^{CO_2} = C_s^{CO_2}\left(T, P_f, C_f^{CO_2}\right) \end{cases} \qquad (8)$$

where T is the temperature (K).

2D lithium isotope and carbonation model. The conceptual 2D modelling of the concentration evolution of lithium isotopes and carbon is based on hydrochemical coupling by solving equations (7) and (8) in 2D. Two non-dimensional numbers

are important for the model: (1) The Rayleigh number (set to 10^6) describes buoyancy effects within the system due to the linear dependence of the fluid density on CO_2 concentration. This controls the homogenization of the fluid composition in the fluid reservoir and the flux from the vein into the ophiolite. (2) The Peclet number (set to 10) describes the ratio between the basal flux and the carbon homogenization rate by diffusion. The ^6Li and ^7Li concentrations are modelled by advection–diffusion identical to the equation used for CO_2 (top row in equation (7)), but with different diffusion (D; Supplementary Methods 3.1) and fluid–rock partition coefficients (K_D; Supplementary Methods 3.2). The permeability was set to be 10^3 times higher in the reservoir and the fault than in the ophiolite. The boundary conditions were set so that the bottom allowed a low fluid flux into the system, whereas the flux out of the system was restricted to the top of the fault. All the other boundaries are zero-flux boundaries, as the top boundary outside the fault, or reflect symmetry conditions (left) or negligible far-field horizontal fluid pressure gradients (right) (Fig. 4b,c). The fluid flux in and out of the system was balanced by setting the fault fluid flux out of the system equal to the basal flux, amplified by the ratio of the width of the base to the width of the fault. Boundary conditions for the concentrations of lithium isotopes and carbon were zero diffusion fluxes normal to all the boundaries. In this way, all the boundary effects were removed based on the concept that there are either no changes in concentration towards infinity (right, top and bottom) or symmetry constraints, which suggests no chemical gradient (left) (Fig. 4b,c).

1D conceptual lithium isotope model. The mass transport efficiency during a reactive fluid flow depends on the magnitude of the fluid–solid partitioning during the mineral replacement reaction, that is, the flux of those elements that preferentially partition into the solid phase is subject to chemical retardation relative to a hypothetical perfectly inert fluid and also to those elements that preferentially partition into the fluid phase. Our equilibrium thermodynamic model indicates that the soapstone carbon concentration is approximately ten times higher than that in the respective equilibrium fluid. In contrast, the available partition coefficients indicate that lithium preferentially partitions into the fluid and the resulting equilibrium solid-phase concentration is typically low. During the alteration, lithium is released into the fluid phase due to the dissolution of lithium-bearing antigorite and subsequently incorporated into secondary talc and chlorite (Supplementary Table 4). As the mineral replacement reaction at the propagating front is driven by carbon, which is subject to chemical retardation, lithium released by the reaction is transported downstream faster than the front propagates, and thus cannot be incorporated in talc and chlorite that precipitate at the front. Consequently, the distribution of lithium isotopes in the soapstone reaction selvage (Fig. 4a and Supplementary Table 3) cannot be related to processes that occur in the outcrop during the reaction front propagation, but instead is linked to reactions that occur on a larger scale to allow for the development of a systematic trend with time. The consistent occurrence of pervasively altered serpentinite at the tectonic contact between the ophiolite and the underlying metasediments indicates that such a large-scale lithium isotope exchange occurred during accumulation of the alteration fluid below the basal thrust (Fig. 2b). Diffusive lithium isotope exchange will take place between lithium-bearing antigorite dehydration fluid and relatively lithium-poor sedimentary pore fluid. Thus, we defined a conceptual lithium isotope diffusion model as:

$$\frac{\partial c^{6,7Li}}{\partial t} = \frac{\partial}{\partial x}\left(\varphi D^{6,7Li}\frac{\partial c^{6,7Li}}{\partial x}\right) \tag{9}$$

where $c^{6,7Li}$ and $D^{6,7Li}$ respectively denote the fluid concentrations and diffusion coefficients of ^6Li and ^7Li and φ is the fluid-filled porosity. The ophiolite porosity is the depth-extrapolated measured He porosity (0.59%; Supplementary Methods 3.3) and we assumed a 2% porosity for the underlying sedimentary schist, consistent with compositionally similar rocks elsewhere[44]. Diffusion of the two lithium isotopes was calculated separately and in non-dimensional space, following a previous numerical approach[16]. Conversion of the non-dimensional characteristic time (Ω) into real time was done by substituting the available lithium isotope diffusion coefficients $D^{6,7Li}$ (Supplementary Methods 3.1). Subsequently, we adjusted the simulation duration to the real-time alteration duration (τ) as defined by our carbon model by fine-tuning the characteristic diffusion length scale (L):

$$\tau = \frac{\Omega L^2}{D^{6,7Li}} \tag{10}$$

For the best-fit alteration duration of ~20 yr, the characteristic length scale for lithium isotope diffusion equals ~11 m, which translates into a fluid reservoir thickness of ~2.1 m (Extended Data Fig. 5). For a duration of 70 yr, L equals 20.4 m, which results in a reservoir thickness of ~4.6 m. The 2D fluid evolution and flow models depicted in Fig. 4 indicate that advective fluid migration below the basal thrust is predominantly horizontal and thus has only a minor effect on the fluid composition draining into the vertical fracture. Figure 4a shows the fluid compositional evolution of the top part of the fluid reservoir over time (Extended Data Fig. 5).

Discussion of model uncertainty. The accuracy of our local equilibrium reactive transport model depends on the accuracy of estimated alteration temperature,

measured sample distances and mineral volume fractions that constrain the simulated reaction front sharpness and propagation distance. The alteration pressure is linked to the alteration temperature assuming a thermobaric gradient of $1 \pm 0.16 \times 10^{-1}\,°C\,bar^{-1}$ and both are used to calculate the carbon diffusion coefficient. Our preferred alteration temperature is $300\,°C$, based on the previously estimated temperature from the same outcrop[28], which is consistent with the greenschist facies metamorphic conditions of the regional Köli Nappe and the recognition of antigorite and talc as a low-grade greenschist metamorphic assemblage in ophiolite occurrences of the Scandinavian Caledonides[55]. Furthermore, the modelled bulk rock composition and mineral abundance and composition of individual phases derived from our equilibrium thermodynamic calculations are in excellent agreement with the measured data from our samples, which corroborates the temperature estimate (Fig. 3b and Extended Data Fig. 2)[28]. Nevertheless, we adopted a conservative uncertainty of $300 \pm 60\,°C$ for the uncertainty propagation of all the temperature-dependent model input parameters. The relatively short length scale of our sample profile allows for precise distance measurements in the field (estimated uncertainty ±0.005 m). However, the bulk rock chemical composition and mineral abundance were obtained from crushed drill cores and hence we adopted a distance uncertainty equivalent to the drill core diameter of 4.5 cm (±2.25 cm), which is smaller than the symbol size in Fig. 3c. For the mineral abundance estimates by TIMA (TESCAN integrated mineral analyser) phase map image analysis, we adopted a conservative distance uncertainty of 4.2 cm (±2.1 cm), equivalent to the thin-section half width measured from both ends. For the measured bulk rock mineral abundance data by X-ray diffraction and TIMA, we estimated uncertainties of 10 vol% and 5 vol%, respectively.

By propagating the conservative uncertainty estimate of 20% for the alteration temperature ($300 \pm 60\,°C$) through the equations that relate carbon diffusivity to temperature and pressure and considering further the 12.8% uncertainty of the molecular dynamics fit[68], we constrained the alteration duration to $19.4 \pm^{8.8}_{5.1}$ yr. We explored further the maximum alteration duration by using the lowest possible $D^{CO_2} = 1.06 \times 10^{-8}\,m^2\,s^{-1}$ ($D^{CO_2} = 1.54 \pm^{0.56}_{0.48} \times 10^{-8}\,m^2\,s^{-1}$; Supplementary Methods 3.1) to fit the modelled antigorite abundance to the extreme ends of the conservative distance and mineral abundance uncertainties. This approach yields the unlikely maximum alteration duration of 115.1 yr. Based on these duration uncertainties, we also evaluated the calculated transient permeability. For the best-fit duration, the equivalent permeability is $2.91 \pm^{1.05}_{0.91} \times 10^{-15}\,m^2$ and the most conservative permeability estimate, based on the longest possible alteration duration, is $0.5 \times 10^{-15}\,m^2$.

Data availability
The authors declare that all the necessary data supporting the findings of this study are available in the article and its Supplementary Information files. Any further data are available from the corresponding authors upon request.

Code availability
The MATLAB reactive transport code is available from the corresponding authors upon reasonable request.

References
51. Lindahl, I. & Nilsson, L. P. in *Geology for Society: Geological Survey of Norway Special Publication* Vol. 11 (ed. Slagstad, T.) 19–35 (Geological Survey of Norway, 2008).
52. Bergman, S. & Sjöström, H. Accretion and lateral extension in an orogenic wedge: evidence from a segment of the Seve–Köli terrane boundary, central Scandinavian Caledonides. *J. Struct. Geol.* **19**, 1073–1091 (1997).
53. Greiling, R. O., Garfunkel, Z. & Zachrisson, E. The orogenic wedge in the central Scandinavian Caledonides: Scandian structural evolution and possible influence on the foreland basin. *GFF* **120**, 181–190 (1998).
54. Beckholmen, M. Geology of the Nordhallen–Duved–Greningen area in Jämtland, central Swedish Caledonides. *Geol. Fören. Stock. För.* **100**, 335–347 (1978).
55. Bucher-Nurminen, K. Mantle fragments in the Scandinavian Caledonides. *Tectonophysics* **190**, 173–192 (1991).
56. Klein, F. & McCollom, T. M. From serpentinization to carbonation: new insights from a CO_2 injection experiment. *Earth Planet. Sci. Lett.* **379**, 137–145 (2013).
57. Klein, F. & Garrido, C. J. Thermodynamic constraints on mineral carbonation of serpentinized peridotite. *Lithos* **126**, 147–160 (2011).
58. Holland, T. J. B. & Powell, R. An internally consistent thermodynamic data set for phases of petrological interest. *J. Metamorph. Geol.* **16**, 309–343 (1998).
59. Holland, T. J. B., Baker, J. & Powell, R. Mixing properties and activity–composition relationships of chlorites in the system MgO–FeO–Al$_2$O$_3$–SiO$_2$–H$_2$O. *Eur. J. Mineral.* **10**, 395–406 (1998).
60. Dale, J., Powell, R., White, R. W., Elmer, F. L. & Holland, T. J. B. A thermodynamic model for Ca–Na clinoamphiboles in Na$_2$O–CaO–FeO–MgO–Al$_2$O$_3$–SiO$_2$–H$_2$O–O for petrological calculations. *J. Metamorph. Geol.* **23**, 771–791 (2005).

61. Green, E., Holland, T. J. B. & Powell, R. An order–disorder model for omphacitic pyroxenes in the system jadeite–diopside–hedenbergite–acmite, with applications to eclogitic rocks. *Am. Mineral.* **92**, 1181–1189 (2007).

62. Padrón-Navarta, J. A. et al. Tschermak's substitution in antigorite and consequences for phase relations and water liberation in high-grade serpentinites. *Lithos* **178**, 186–196 (2013).

63. Aranovich, L. Y. & Newton, R. C. Experimental determination of CO_2–H_2O activity-composition relations at 600–1000 °C and 6–14 kbar by reversed decarbonation and dehydration reactions. *Am. Mineral.* **84**, 1319–1332 (1999).

64. Holland, T. J. B. & Powell, R. A compensated-Redlich–Kwong (CORK) equation for volumes and fugacities of CO_2 and H_2O in the range 1 bar to 50 kbar and 100–1600 °C. *Contrib. Mineral. Petrol.* **109**, 265–273 (1991).

65. Manning, C. E. The solubility of quartz in H_2O in the lower crust and upper mantle. *Geochim. Cosmochim. Acta* **58**, 4831–4839 (1994).

66. Vrijmoed, J. C. & Podladchikov, Y. Y. Thermodynamic equilibrium at heterogeneous pressure. *Contrib. Mineral. Petrol.* **170**, 10 (2015).

67. Plümper, O., John, T., Podladchikov, Y. Y., Vrijmoed, J. C. & Scambelluri, M. Fluid escape from subduction zones controlled by channel-forming reactive porosity. *Nat. Geosci.* **10**, 150–156 (2017).

68. Moultos, O. A., Tsimpanogiannis, I. N., Panagiotopoulos, A. Z. & Economou, I. G. Self-diffusion coefficients of the binary ($H_2O + CO_2$) mixture at high temperatures and pressures. *J. Chem. Thermodyn.* **93**, 424–429 (2016).

Author contributions

A.B. designed the study, conducted the fieldwork with M.T. and performed the petrography and chemical analyses. T.M. conducted the bulk rock analyses of the lithium concentration and isotopes. A.B., Y.Y.P., J.C.V. and T.J. developed the model and A.B. wrote the manuscript with important contributions from all the co-authors.

Competing interests

The authors declare no competing interests.

Additional information

Extended data is available for this paper at https://doi.org/10.1038/s41561-020-0554-9.

**Supplementary information** is available for this paper at https://doi.org/10.1038/s41561-020-0554-9.

Correspondence and requests for materials should be addressed to A.B. or T.J.

**Peer review information** Primary Handling Editor: Rebecca Neely.

**Reprints and permissions information** is available at www.nature.com/reprints.
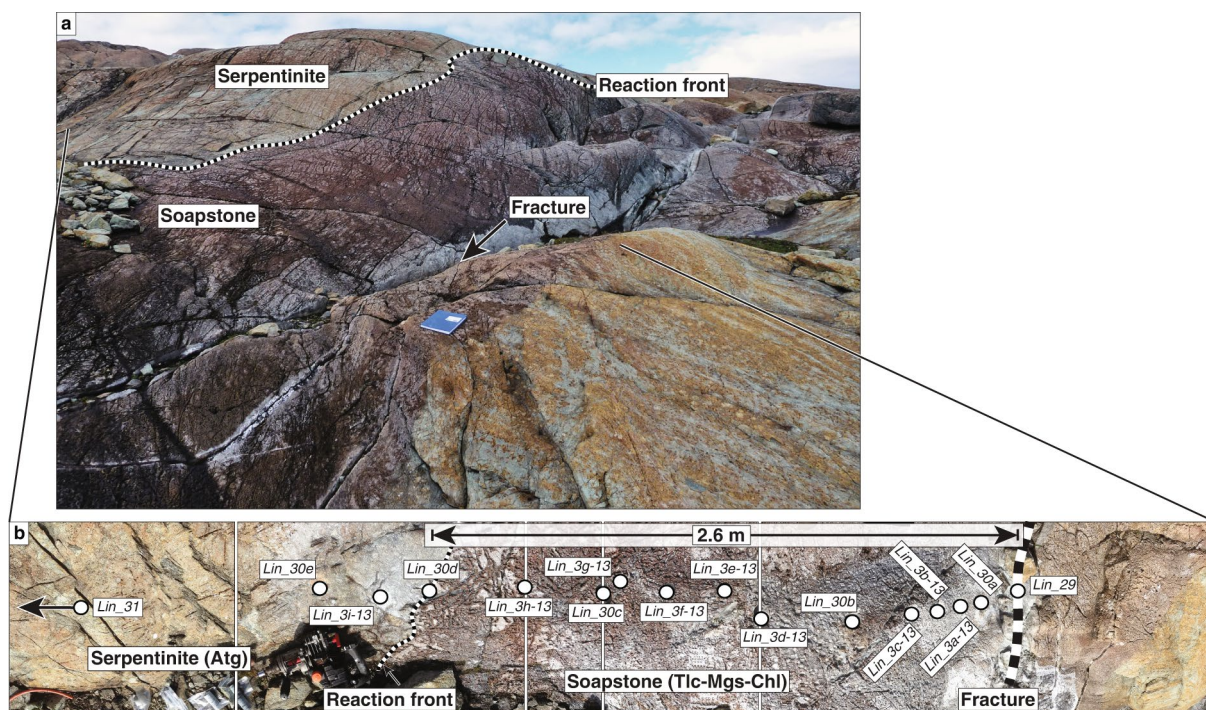
Extended Data Fig. 1 | Field relationships in outcrop. a, The investigated soapstone reaction selvage around a central fracture in serpentinite. The fracture now contains mostly talc together with minor magnesite and dolomite. The red-brown color of the soapstone is caused by a thin (~2 mm) weathering layer. **b**, Composite image showing details of sample locations along the sampling traverse with respect to the fracture and soapstone–serpentinite reaction interface. Note that this image is not to scale due to distortion effects. Distances between samples and the fracture and reaction front have been measured in the field. The location of the least altered serpentinite sample Lin_31 is outside the image, 2.4 m from the reaction front on the left hand side. The picture was taken during fieldwork 2013 and kindly provided by Harrison Lisabeth.
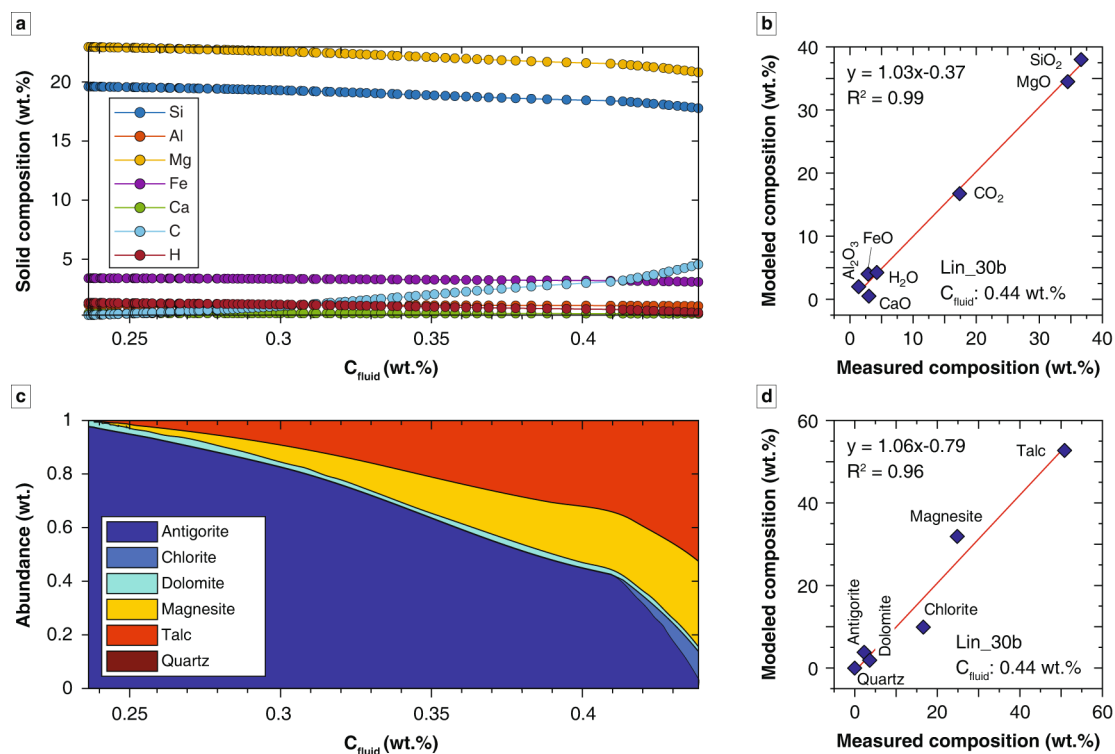
Extended Data Fig. 2 | Local equilibrium thermodynamic model of bulk system composition. a, Relation between the bulk rock major element composition and pore fluid carbon concentration. **b**, Measured bulk rock composition of sample Lin_30b (Supplementary Table 2) compared with the modeled bulk rock composition at pore fluid carbon concentration of 0.44 wt.%. **c**, Modeled total mineral abundance variation for the bulk system composition shown in Extended Data Fig. 2a. **d**, Measured bulk rock phase proportions of sample Lin_30b (Supplementary Table 1) compared with the modeled bulk rock phase proportions at pore fluid carbon concentration of 0.44 wt.%.
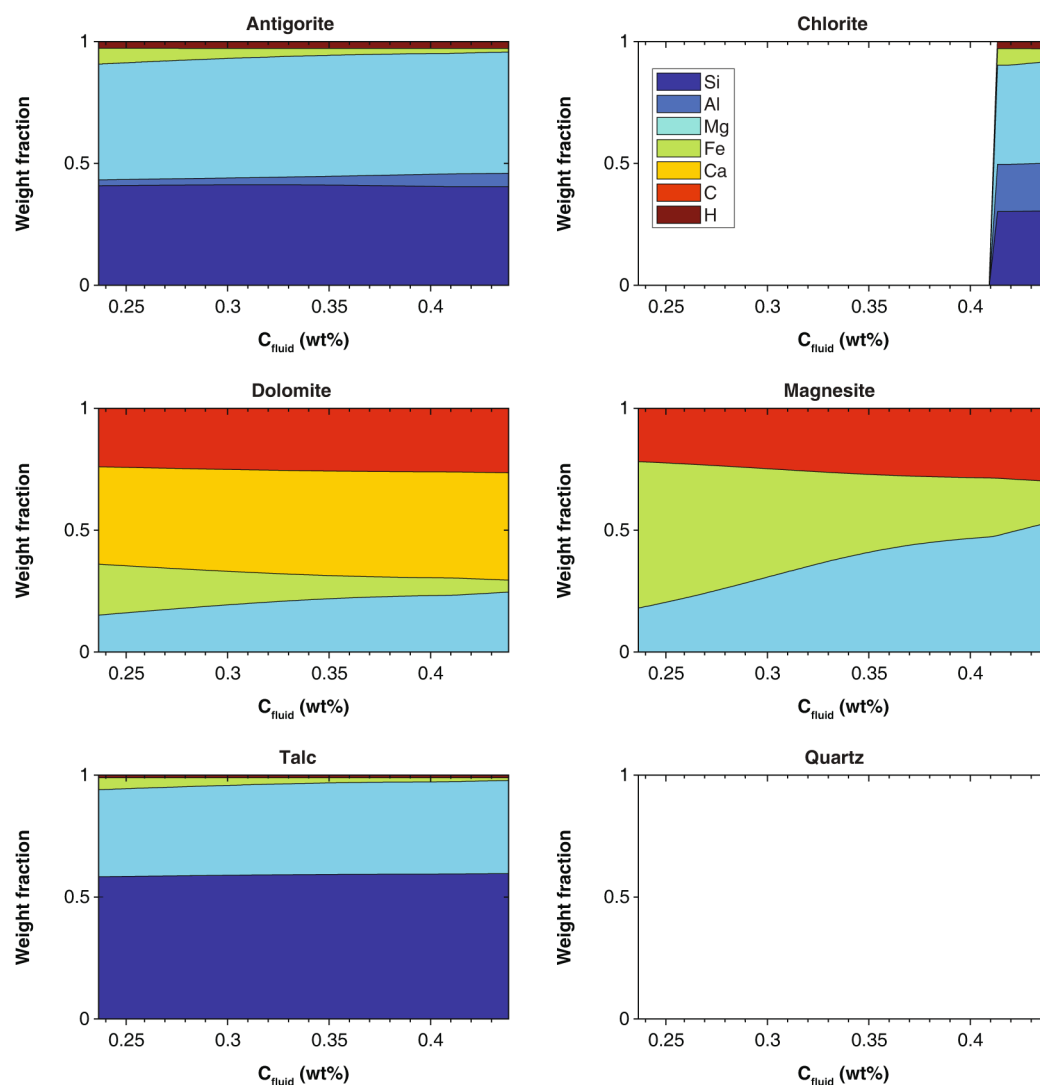
Extended Data Fig. 3 | Modeled system phase composition. Plots showing the mineral compositional evolution with increasing pore fluid carbon concentration. Note that the model predicts the absence of quartz from the alteration assemblage consistent with the sample composition.
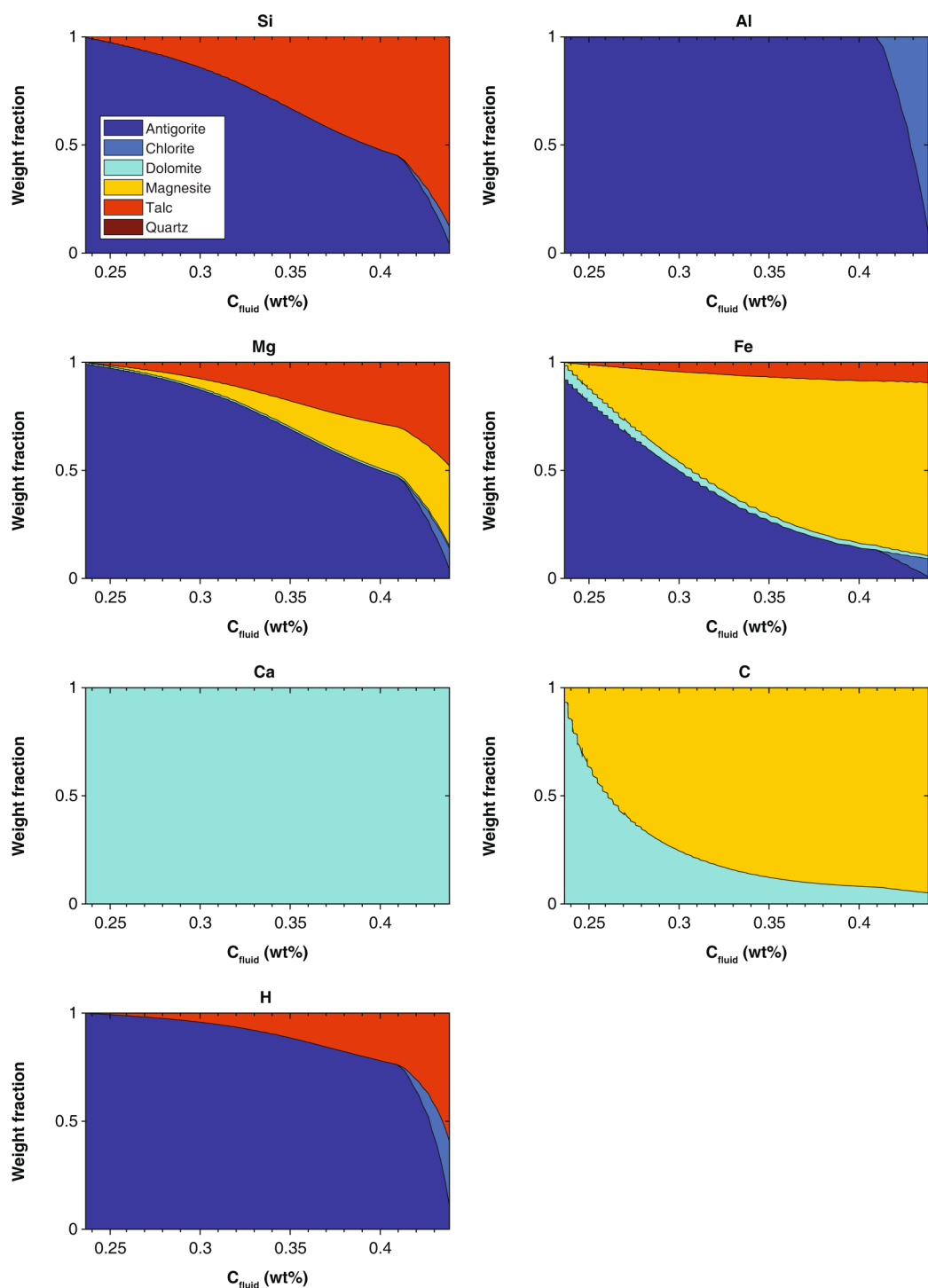
Extended Data Fig. 4 | Modeled system component distribution. Plots showing the modeled distribution of major elements among the mineral phases for different pore fluid carbon concentrations.
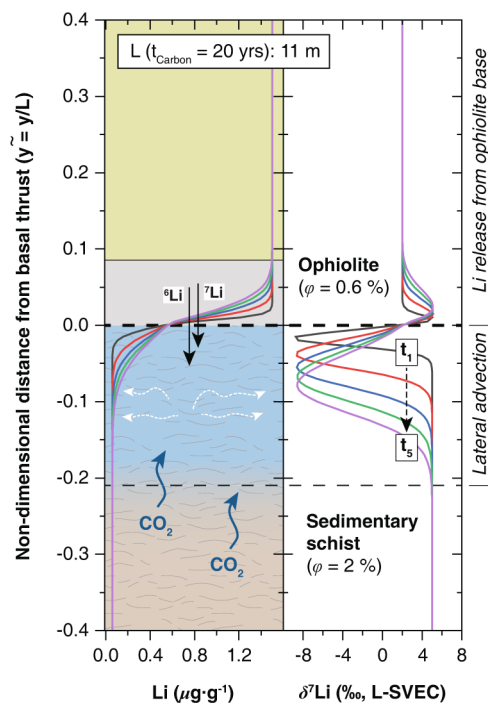
Extended Data Fig. 5 | Conceptual lithium concentration and isotope ratio evolution of the alteration fluid reservoir. Incipient carbonation of the lowermost part of the ophiolite upon alteration fluid accumulation below the basal thrust results in lithium isotope release due to replacement of serpentinite by secondary soapstone. The different colors depict distinct time steps from early (t_1) to late (t_5) and show the lithium concentration and isotope ratio (δ^7Li) evolution. Pore fluid from the uppermost part of the basal sedimentary schist laterally drains into ophiolite internal fractures, driving the formation of soapstone alteration selvages (see also Figs. 2b and 4b,c). Lateral fluid advection will have only a small effect on the lithium isotope composition. The model fit to the duration obtained from the carbon reactive transport simulation defines the characteristic diffusion length scale of 11 m and thus constrains the thickness of the drainage layer (y) to ~2.1 m below the basal thrust.